MOF-derived Co/Fe@NPC-500 with large amounts of low-valent metals as an electro-Fenton cathode for efficient degradation of ceftazidime

Hexiang Wang [a], Chenliu Tang [a], Luwei Wang [a], Zhirong Sun [b], Xiang Hu [a,*]

[a] *Research Group of Water Pollution Control and Water Reclamation, College of Chemical Engineering, Beijing University of Chemical Technology, Beijing 100029, PR China*
[b] *Faculty of Environment and Life, Beijing University of Technology, Beijing 100124, PR China*
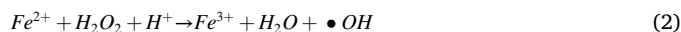
ARTICLE INFO

ABSTRACT

A MOF-derived carbon material containing CoFe alloy (Co/Fe@NPC-500) by calcining N-doped Co/Fe bimetallic MOF at a lower temperature was successfully synthesized as a cathode in electro-Fenton process for ceftazidime (CAZ) degradation. The presence of Co could accelerate the transfer of electrons from C atoms of carbon material to Fe, thus increasing the content of low-valent metals in the material, which had been demonstrated by characterizations and density functional theory (DFT) calculations. Thanks to the integrity of the MOF structure, the synergistic effect between Fe and Co, Co/Fe@NPC-500 cathode showed efficient removal efficiency for CAZ completely removed within 60 min and obtained a total organic carbon (TOC) removal rate of 52.1% at 90 min. Besides, based on the results of HPLC-MS and DFT calculations, the degradation pathway of CAZ was proposed. This study provides some useful information for the preparation of MOF-derived carbon materials containing low-valent metals for electro-Fenton process.

1. Introduction

Residual antibiotics in the environment can not only contaminate food and drinking water but also accelerate the evolution of antibiotic resistant genes and antibiotic resistant bacteria, which pose a growing threat to humans and ecosystems [1]. Ceftazidime (CAZ), an antibiotic commonly used to treat intestinal, abdominal, and respiratory infections, could cause chromium toxicity in organisms and promote the development of resistant genes when it enters the natural environment [2]. Unfortunately, it has been detected in the natural environment, because antibiotics are chemically stable and low biodegradability making them difficult to remove by traditional treatment techniques such as floatation, gravity and chemical coagulation [3].

Electro-Fenton, a kind of electrochemical advanced oxidation process, is widely applied for the removal of persistent organic pollutants. It is well known that electro-Fenton can activate hydrogen peroxide (H_2O_2) continuously generated by a two-electron oxygen reduction process on the cathode (Eq. (1)) to produce hydroxyl radicals (Eq. (2)) that can have high oxidation potential (E = 2.72 V/NHE) to effectively degrade numerous toxic pollutants [4]. However, the conventional electro-Fenton process was suppressed by limited pH range (<3) and disposal of iron sludge [5]. In order to make electro-Fenton available at a wider pH range and reduce the production of iron sludge, it is necessary to design an efficient heterogeneous electro-Fenton cathode to purify wastewater.

$$O_2 + 2e^- + 2H^+ \rightarrow H_2O_2 \tag{1}$$

$$Fe^{2+} + H_2O_2 + H^+ \rightarrow Fe^{3+} + H_2O + \bullet OH \tag{2}$$

$$Fe^{3+} + e^- \rightarrow Fe^{2+} \tag{3}$$

Metal-organic frameworks (MOFs), also known as porous coordination polymers (PCPs), are constructed by coordination bonds connecting metal-containing inorganic building blocks and polydentate organic ligands into three-dimensional or two-dimensional interconnected networks [6]. By choosing different metal ions or organic ligands, we can easily prepare bimetallic MOF or dope the MOF with different elements. In addition, MOF-derived carbon materials can be synthesized by calcining MOF at high temperatures, which have excellent properties of high surface area, high porosity, adjustable pore size, high conductivity and stability [7]. Many recent studies have carbonized MOF materials directly at high temperatures to obtain metals or metal oxides, which can be used as an alternative method to synthesize porous functional materials applied to heterogeneous electro-Fenton [5,8]. However, most

---

iron-based MOFs contain only Fe(III), which back affect the activity of the Fenton reaction [9]. Although Fe(III) can be reduced to Fe(II) in the material with the presence of carbon after high temperature carbonization [10], the high carbonization temperature will cause complete thermal decomposition of the MOF and lead to a decrease in surface area and inactivation of the active metal sites, thus losing the advantages of the original MOF [11]. Therefore, how to obtain more low-valent metals while maintaining the MOF structure is an urgent problem to be solved.

If we want to keep the good structure of the original MOF, low temperature calcination is an effective method. However, MOF-derived carbon materials prepared by low temperature calcination have two problems: (1) Their conductivities were very low, which could slow down the reduction of Fe(III) to Fe(II), because the reduction can be electrochemically driven (Eq. (3)) [12]; (2) The proportion of high-valent metals is very large, which will also slow down the Fenton reaction. Nitrogen doping is an effective method to reduce interface transfer resistance because the introduction of nitrogen causes the formation of asymmetric spin density and inhomogeneous charge distribution in the carbon plane [13]. In addition, different types of transition metals with significant catalytic ability can be introduced to accelerate the Fenton reaction. Among them, the cobalt-based catalysts not only have a similar role as iron-based catalysts in Fenton catalysis but also have high oxygen reduction activity [9]. It is more important that Co/Fe bimetallic materials could form alloy during the calcination process, which is conducive to reducing Fe^{3+}/Co^{3+} into Fe^{2+}/Co^{2+}, thus increasing the content of low-valent metals in the catalyst. Moreover, this conversion will also occur in the Fenton reaction process [14].

In this study, MOF-derived carbon material containing CoFe alloy (Co/Fe@NPC) by calcining N-doped Co/Fe bimetallic MOF at a lower temperature was successfully synthesized. The presence of CoFe alloy would be beneficial to increase the content of low-valent metals in the catalyst and accelerate the Fenton reaction. The properties of MOF-derived carbon materials were characterized, and the catalytic activity and stability of Co/Fe@NPC were investigated for CAZ degradation in electro-Fenton systems. Additionally, the degradation mechanism and pathway of CAZ were also presented. This work provides some useful information for the preparation of MOF-derived carbon materials containing low-valent metals for electro-Fenton process.

2. Experimental section

2.1. Material and chemicals

Terephthalic acid (H_2BDC, AR), 2-Aminoterephthalic Acid (NH_2-BDC, AR), tert-butanol (TBA), methanol (CH_3CH_2OH, AR), ethanol (CH_3OH, AR), 5,5-dimethyl-1-pyrroline-N-oxide (DMPO, AR), 2,2,6,6-tetramethylpiperidine (TEMP, AR) and polytetrafluoroethylene (PTFE, 60 wt%) were obtained from Aladdin (Shanghai, China). Cobalt nitrate hexahydrate ($Co(NO_3)_2 \cdot 6 H_2O$, AR), Iron (III) chloride hexahydrate ($FeCl_3 \cdot 6 H_2O$, AR), N,N-dimethylformamide (DMF, AR), potassium hexacyanoferrate ($K_3Fe(CN)_6$, AR), potassium dihydrogen phosphate (KH_2PO_4, AR) were purchased from Beijing Chemical Works (Beijing, China). CAZ was purchased from National Institutes for Food and Drug Control (Beijing, China). All aqueous solutions for analyses, as well as synthetic gemfibrozil solutions, were prepared with Millipore Milli-Q water ($\rho > 18.2$ MΩ cm).

2.2. Preparation of MOF

The Co/Fe-N-MOF was synthesized by mixing 2.5 mmol $FeCl_3 \cdot 6 H_2O$, 5 mmol $Co(NO_3)_2 \cdot 6 H_2O$, 7.5 mmol NH_2-BDC and 60 mL DMF in 100 mL Taflon-lined stainless autoclave which was sealed and maintained as 110 °C for 20 h. The precipitate was collected by centrifugation, sequentially washed with DMF and ethanol for 3 times. The Fe-N-MOF and Co-N-MOF were prepared in the same procedure as the preparation of the Co/Fe-N-MOF except using bare $FeCl_3 \cdot 6 H_2O$ and Co

$(NO_3)_2 \cdot H_2O$, respectively. Besides, the Co/Fe-MOF without nitrogen was also synthesized by using H_2BDC as an organic ligand.

2.3. Preparation of MOF-derived carbon materials

The Co/Fe-N-MOF was put in a tube furnace and heated to different calcination temperature (400, 500, 600 and 700 °C) for 3 h under N_2 atmosphere with a heating rate of 5 °C min^{-1} to produce Co/Fe@NPC-400, Co/Fe@NPC-500, Co/Fe@NPC-600 and Co/Fe@NPC-700 (NPC = N-doped porous carbon), respectively. Similarly, the Co/Fe-MOF, Fe-N-MOF, and Co-N-MOF were calcined at 500 °C for 3 h under N_2 atmosphere and named as Co/Fe@PC-500 (PC = porous carbon), Fe@NPC-500 and Co@NPC-500, respectively.

2.4. Preparation of MOF-derived carbon material electrode

The Co/Fe@NPC-500 cathode was prepared as flow: 50 mg CB and 20 μL 60 wt% PTFE were dispersed in 20 mL ethanol, and ultrasonically stirred for 0.5 h. Then, the above solution was stirred vigorously at 80 °C until a wet paste was obtained. The resulting paste was coated on the side of the stainless-steel mesh. Similarly, the wet paste of the Co/Fe@NPC-500 was made in the same way and coated on the other side of the stainless-steel mesh. After drying at 80 °C, the Co/Fe@NPC-500 electrode was acquired. For comparison, other MOF-derived carbon materials were also made into electrodes via the same process.

2.5. Characterizations

The surface morphologies and surface elemental mapping of material were performed using a scanning electron microscopy (SEM) with energy dispersive X-ray analysis (EDS) (TESCAN MIRA LMS, Czech). Powder X-ray diffraction (XRD) analysis was performed using a Rigaku SmartLab SE (Shimadzu, Japan) with a Cu K α radiation source at 40 kV and 200 mA. X-ray photoelectron spectroscopy (XPS) analysis was carried out using Thermo Scientific K-Alpha with a monochromatic Al Kα X-ray source at 12 kV and 6 mA. Thermo Scientific Nicolet iS20 and HORIBA Scientific LabRAM HR Evolution were used to perform the Fourier transform infrared spectra (FT-IR) and Raman spectra. Brunauer–Emmett–Teller (BET) specific areas were determined using a Micromeritics ASAP 2020 (USA). Thermogravimetric analysis (TGA) was carried out with Hitachi TG/DTA 6300 (Japan) between 20 and 800 °C at a heating rate of 5 °C min^{-1} under N_2 atmosphere. Hydrophilicity property of the electrode was characterized by the drop shape analysis system (Kruss DSA 100 S, Germany).

The electrochemical measurements were performed in a three-electrode system with an electrochemical workstation (CHI660E, Chenhua Instruments). A Pt wire and saturated calomel electrode (SCE) were used as counter electrode and reference electrode, respectively. The working electrode was prepared as following: 10 mg catalyst and 20 μL Nafion solution (5 wt%) were dispersed in 1 mL ethanol aqueous solution (50%) to form a homogeneous ink by ultrasonic oscillation for 30 min. Then 8 μL ink was dropped on the glassy carbon electrode surface and dried at room temperature. The oxygen reduction activity was investigated by cyclic voltammetry (CV) in O_2/N_2-saturated electrolyte Na_2SO_4 solution with a scan rate of 5 mV s^{-1}. The electrochemical impedance spectroscopy (EIS) analyses were performed at open circuit potential in the frequency range from 1 Hz to 100 kHz in 0.05 mol L^{-1} Na_2SO_4 solution. The electrochemical surface area (ECSA) of the working electrode was calculated by CV test in 10 mmol L^{-1} potassium ferricyanide and 0.1 mol L^{-1} KCl and quantified by the Randles-Sevcik equation (Eq. (4)).

$$i_p = 2.69 \times 10^5 n^{\frac{3}{2}} ACD^{\frac{1}{2}} v^{\frac{1}{2}} \tag{4}$$

where I_p is the peak current (A), n is the number of electrons transferred, A is the electroactivity surface area (cm^2), C is the concentration of

potassium ferricyanide (1×10^{-5} mol cm^{-3}), D is the diffusion coefficient (7.6×10^{-6} cm^2 s^{-1}) and ν is the scan rate (V s^{-1}).

2.6. Experimental procedures

The degradations were carried out in an undivided open cylindrical reactor containing 100 mL 5 mg L^{-1} CAZ as the pollutant and 0.05 mmol L^{-1} Na$_2$SO$_4$ as supporting electrolyte. A platinum wire and the MOF-derived carbon material electrode (2 cm $\times$ 3 cm) were used as anode and cathode, respectively. The current was supplied by a DC power supply (DH 1766–2, China). At certain time intervals, 1.0 mL sample was taken and filtered through a 0.22 μm membrane for further analysis. The initial pH value of the system was adjusted with 0.1 mol L^{-1} H$_2$SO$_4$ and 0.1 mol L^{-1} NaOH solution. Each experiment was performed in triplicate to calculate the mean values and error bars.

2.7. Analytic methods

The degradation of CAZ was analyzed by a high-performance liquid chromatograph (HPLC) equipped with an Agilent TC-C18 column (250 mm $\times$ 4.6 mm, 5 μm) and a UV detector setting wavelength at 254 nm. The mobile solution consisted of acetonitrile and 6.8 g L^{-1} KH$_2$PO$_4$ solution (0.125:0.875, v/v) and a flow rate was 1 mL min^{-1} with column temperature of 30 °C. The intermediates were obtained using a high-performance liquid chromatography with mass spectrometry (HPLC-MS) by Xevo G2 Qtof (Waters, USA). The total organic carbon (TOC) was determined with the HTY-CT 1000 M (Tailin, China). The accumulation of H$_2$O$_2$ during the electro-Fenton process was determined using the potassium titanyl oxalate method [15]. The concentration of leached Fe and Co in the solution was determined by inductive coupled plasma-optical emission spectrometry (ICP-OES). To evaluate the feasibility of degradation, energy consumption W (Wh m^{-3}) (Eq. (5)) and electrical energy per order (E$_{EO}$) (Eq. (6)) were calculated [16].

$$W = \frac{UIT}{V} \tag{5}$$

$$E_{EO} = \frac{W}{\log(C_0/C)} \tag{6}$$

where U is voltage (V), I is current (A), T is reaction time (h), V is volume (m^{-3}), C$_0$ is initial concentrations of CAZ (mg L^{-1}) and C$_t$ is final concentrations of CAZ (mg L^{-1}).

2.8. Density functional theory (DFT) calculation

DFT calculations on the three models, Fe$_3$O$_4$, C-O-Fe$_3$O$_4$ and C-O-Co-Fe$_3$O$_4$, were performed by PBE0 functional with def2-TZVP basis set where the auxiliary basis set was def2/J [17,18]. The DFT-D3 method of Grime and coworkers was used to treat dispersion forces [19,20]. To obtain neutral clusters, the dangling bonds were treated using H atoms. Molecular DFT calculations on CAZ were performed using the B3LYP method with 6–31 G(d,p) basis set level and SMD water solvation model [21–23].

Geometry optimization and single-point energy were carried out by ORCA software (Version 5.0.3) [24,25]. The generation of the ORCA input file and post-processing of the data were executed by Multiwfn software [26–28]. DFT calculation results were visualized by VMD software (Version 1.93) [29].

3. Results and discussion

3.1. Morphology and characterizations

The surface morphology of Co/Fe@NPC-500 was observed by SEM (Fig. 1(a-b)). Co/Fe@NPC-500 presented the typical morphology of a bipyramidal hexagonal prism. Besides, there were some spheres attached to the surface of Co/Fe@NPC-500 in Fig. 1(b), indicating that some new materials generated during the calcination process could be uniformly distributed on the surface of Co/Fe@NPC-500 due to the long-range orderly nature of the MOF. Then the EDS elemental mapping suggested uniform distribution of Fe, Co, N and O in Co/Fe@NPC-500 (Fig. 1(c-f)).

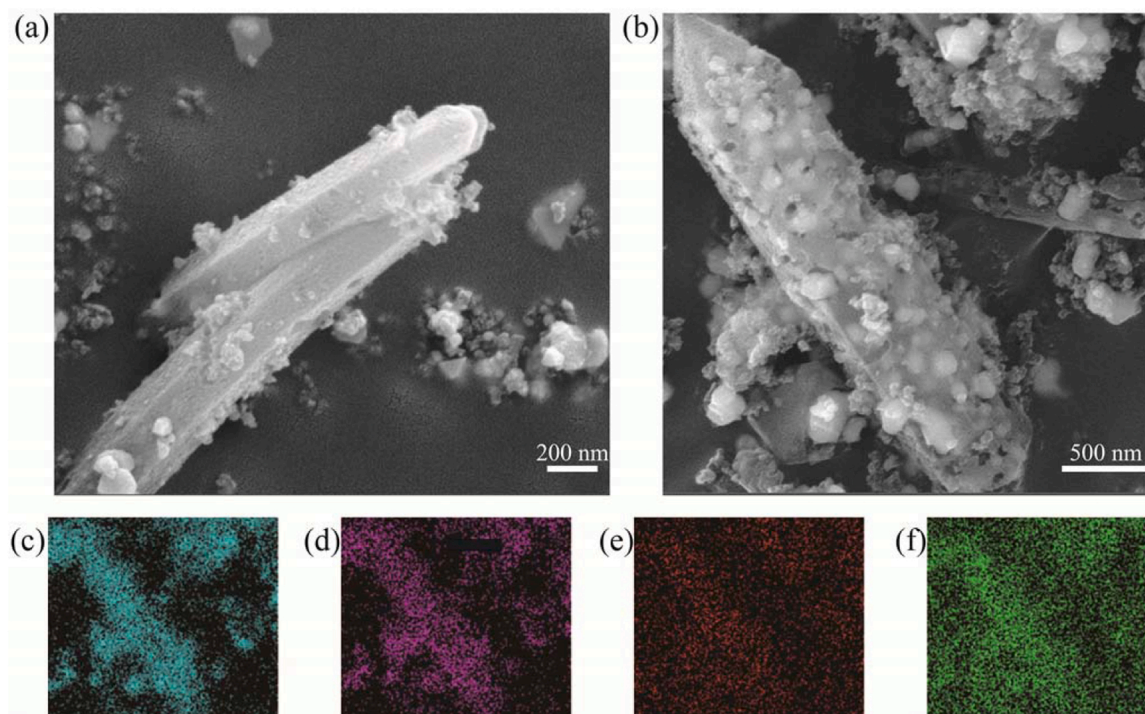The XRD patterns of the different pristine MOFs produced by the

Fig. 1. (a, b) The SEM image of Co/Fe@NPC-500; and the elemental mapping of Fe (c), Co (d), N(e) and O(f).

solvothermal method were shown in Fig. S1. The characteristic peaks at 9.2°, 10.2° and 20° of Fe-N-MOF could be well matched with the single crystal structure data of NH$_2$-MIL-88(Fe) (CCDC 647646) [30], which demonstrated that NH$_2$-MIL-88(Fe) was synthesized. The XRD pattern of Co/Fe-N-MOF did not change significantly compared with that of Fe-N-MOF, indicating that the addition of Co did not change the crystal structure of NH$_2$-MIL-88(Fe). Besides, the XRD pattern of Co/Fe-MOF without NH$_2$-BDC as the organic ligand agreed with the simulated diffraction spectra of MIL-88(B) (CCDC 2088535) [31], where the peaks tended to shift compared with those of MOF with NH$_2$-BDC. The low intensity of the peaks in the XRD pattern of Co-N-MOF showed the low crystallinity of this sample. Those peaks at 6.7° and 11.7° correspond to the (110) and (300) crystallographic planes of Co-MOF-74 (CCDC 1494752) [32], respectively.

As shown in Fig. 2(a), the main component of the Co/Fe@NPC calcinated 400 °C was Fe$_2$O$_3$ (PDF#79–1741), while the characteristic peaks of the pristine MOF all disappeared. At a calcination temperature of 500 °C, the XRD pattern of Co/Fe@NPC had well-matched diffraction at diffraction peaks at 44.8°, 65.2° and 82.6°, corresponding well to CoFe alloy (PDF#44–1433). The transition from Fe$_2$O$_3$ to CoFe alloy indicated that Fe^{3+} in the material was gradually reduced to Fe^0. And it was worth noting that Fe^0 could not only react with H$_2$O$_2$ to form ·OH but also facilitate the reduction from Fe^{3+} to Fe^{2+} thus accelerating the Fenton reaction proceeds [14]. In addition, with the calcination temperature rising, the intensity of the characteristic peaks of CoFe alloy became higher and higher, which also demonstrated the increase in the proportion of Fe^0.

The changes in components and structures of the Co/Fe-MOF during pyrolysis were observed by TGA presented in Fig. S2. When the temperature was raised from 20 to 800 °C, the weight loss of MOF could be divided into 4 stages. Stage 1 was below 360 °C with a weight loss of 30.1%, and this was related to the evaporation of DMF adsorbed on the Co/Fe-MOF [33,34]. Stage 2 was between 360 and 500 °C with a weight loss of 27.8%, which was associated with the formation of metallic oxide and decomposition of organic ligands in the Co/Fe-MOF [35,36]. Stage 3 was from 500 to 530 °C with a weight loss of 3.9%, where the metal oxide was converted to CoFe alloy. This conversion was also reflected in the XRD results. In the final stage (from 530 to 800 °C), the MOF-derived carbon material was slowly pyrolyzed due to the increase in temperature [37]. From the results of TGA, it could be concluded that the calcination temperature should be set at 500 °C to obtain CoFe alloy while maintaining a certain MOF structure.

The characteristic peaks of Fe@NPC-500 at 30°, 35.4° and 65.5° correspond to the (220), (311) and (440) crystal planes of this Fe$_3$O$_4$ (PDF#89–2355), respectively (Fig. 2(b)). Comparing the main compositions of Fe@NPC-500 and Co/Fe@NPC-500, we could find that the presence of Co helped the conversion of the high-valent metal to the low-valent metal, and such conversion was beneficial to the Fenton reaction.

Besides, the doping of nitrogen had less effect on the metal valent state from the fact that the main components of Co/Fe@NPC-500 and Co/Fe@PC-500 were the same.

XPS analysis was performed to reveal the surface composition, chemical state and binding energy of Co/Fe@NPC-500 in Fig. S3. The survey pattern verified the presence of the C, N, O, Fe and Co elements (Fig. S3a). The three characteristic peaks observed in the C 1 s spectrum (Fig. S3b) could be assigned to C-C (284.8 eV), C-O (285.6 eV), and C=O (289.4 eV) [38]. As shown in Fig. S3c, the characteristic peaks at 530.0, 532.2 and 538.1 eV were the lattice oxygen, surface oxygen and adsorbed oxygen of the catalyst, respectively, which were consistent with the appearance of the characteristic peaks of C-O and C=O in the C 1 s spectrum [39]. It could be seen from the peak area that the percentage of surface oxygen (88%) was much higher than that of lattice oxygen (9%), which could be due to the fact that the main component of Co/Fe@NPC-500 was CoFe alloy rather than metal oxide. It had also been reported that surface oxygen often contains oxygen vacancies, oxygen-containing functional groups and other substances that contributed to the ORR reaction [9]. The N 1 s spectrum contained three peaks to reveal the presence of pyridinic-N (398.7 eV), pyrrolic-N (400.4 eV) and pyridine oxide nitrogen (404.2 eV) [40]. Since the electronegativity of nitrogen is higher than that of carbon, the carbon atoms near the nitrogen atoms have a higher density of positive charges to counteract the strong electrophilicity of the nitrogen atoms, which can facilitate the adsorption of oxygen, superoxide and hydroperoxides [41]. Fe 2p spectrum of Co/Fe@NPC-500 (Fig. S3e) could be divided into eight characteristic peaks, which were Fe^0 (707.1 and 720.0 eV), Fe^{2+} (710.5 and 723.3 eV), Fe^{3+} (713.2 and 726.8 eV) and satellite peaks (714.0 and 729.0 eV) [42]. The characteristic peaks of Fe^0 coincided with the appearance of CoFe alloy in the XRD pattern. Similarly, the Co 2p spectrum (Fig. S3f) can be deconvoluted to show six peaks for Co^0 (778.5 and 793.2 eV), Co^{2+} (781.0 and 795.1 eV) Co-N(784.1 and 799.88 eV) and satellite peaks (787.5 and 801.6 eV), respectively [43, 44].

Fig. 3(a) showed the variation of iron on the surface of Co/Fe@NPC catalysts at different calcination temperatures, where the valent state of Fe was predominantly divalent and trivalent at 400 °C. When the calcination temperature was raised to 500 °C, the radio of Fe^{2+} and Fe^{3+} started to decrease (from 0.33 to 0.24 for Fe^{3+} and from 0.67 to 0.55 for Fe^{2+}). The trend was consistent with the results of XRD that the intensity of characteristic peaks of CoFe alloy gradually strengthened with the increase of calcination temperature owing to the carbon in the catalyst as a reducing agent at high temperatures. However, the high temperature could cause the collapse of the MOF derivative structure where the active sites could be obscured [45], which was supported by the decreasing intensity of the Fe 2p spectra as the calcination temperature increased. Similarly, as shown in Fig. S4, Co/Fe@NPC calcined at 400 °C was mainly in the form of Co^{2+} while Co^0 appeared at 500 °C. Besides
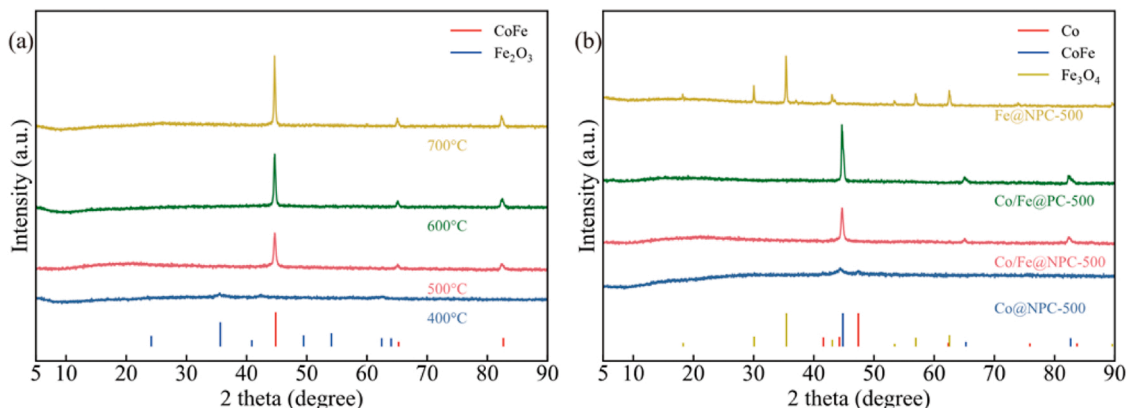

Fig. 2. XRD patterns of (a) Co/Fe@NPC calcinated at different temperatures and (b) Fe@NPC-500, Co/Fe@NPC-500, Co/Fe@PC-500, Co@PC-500.
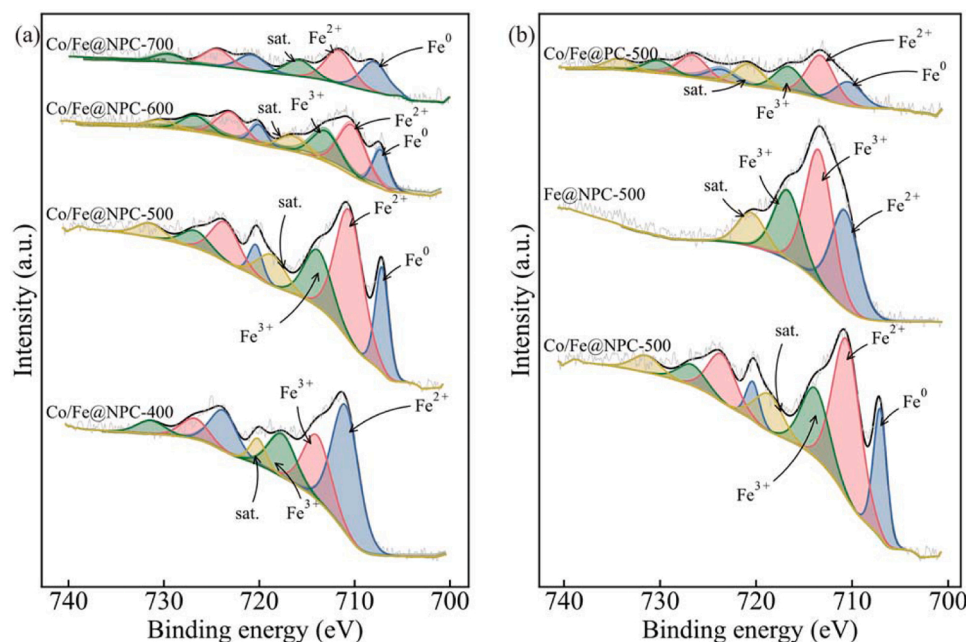
Fig. 3. High-resolution scanning XPS spectra for Fe 2p of (a) Co/Fe@NPC calcinated at different temperatures and (b) Fe@NPC-500, Co/Fe@NPC-500, Co/Fe@PC-500.

the percentage of Co^0 continued to increase as the calcination temperature continued to increase. The lack of Co^{3+} in the MOF derivatives could be due to the lower content of Co^{3+} which is thermodynamically easier to electronically convert to Co^{2+}. As described in Fig. 3(b) and Fig. S5, we could see that the doping of nitrogen had no significant effect on the valent state of Fe, while the addition of Co caused the valent state of Fe to shift from Fe^{3+} and Fe^{2+} to Fe^0, which provided a possibility to obtain more low-valent metals without collapse of the structure of MOF derivatives by low temperature calcination. The presence of Fe^0 facilitated the cycling of Fe^{3+} to Fe^{2+} and accelerated the Fenton reaction [14].

As shown in Fig. 4(a), the Raman spectra of Co/Fe@NPC-500, Fe@NPC-500, and Co@NPC-500 displayed two major bands at 1320 and 1585 cm^{-1}. The D Band, at 1320 cm^{-1}, reflected the structural defects or disordered structure at the edges of the carbon material. G band, at 1585 cm^{-1}, correlated with the degree of graphitization of the carbon material. A smaller intensity ratio between D and G bands (I_D/I_G) was reported to indicate a relatively high graphitization level which would improve electrical conductivity [46]. The I_D/I_G value of Co/Fe@NPC-500, Fe@NPC-500, Co@NPC-500 were 0.88, 0.91 and

1.00, suggesting that the synergistic interaction between Fe and Co could improve the graphitization of the material and reduce the defect points.

The FT-IR spectra of the materials were studied to illustrate the effect of doping and calcination temperature on the structure of MOF derivatives. As displayed in Fig. 4(b), the characteristic peaks at 1600–1300 cm^{-1} could be attributed to the asymmetric and symmetric stretching vibrations of C-O/C=O, which confirmed the presence of dicarboxylic acid-linked ligands in the material [11]. The peak at 745 cm^{-1} belonged to the C-H stretching vibration of the benzene ring [47]. And the vibration at 580 can be attributed to the vibration of Fe-O, indicating the formation of the Fe coordination with the ligands [48]. Due to the absence of Fe, The FT-IR spectra of Co@NPC-500 didn't have the characteristic peak at 580 cm^{-1} likely that of Fe@NPC-500. In addition, the intensity of the other characteristic peaks of Co@NPC-500 was significantly lower than those of the other two materials, which could be due to the low crystallinity of the original Co-N-MOF. Fig. 4(b) also showed the FT-IR of Co/Fe@NPC-700 after calcination at 700 °C where all the strong peaks weaken or disappeared, meaning that the organic ligands were completely decomposed during the carbonization
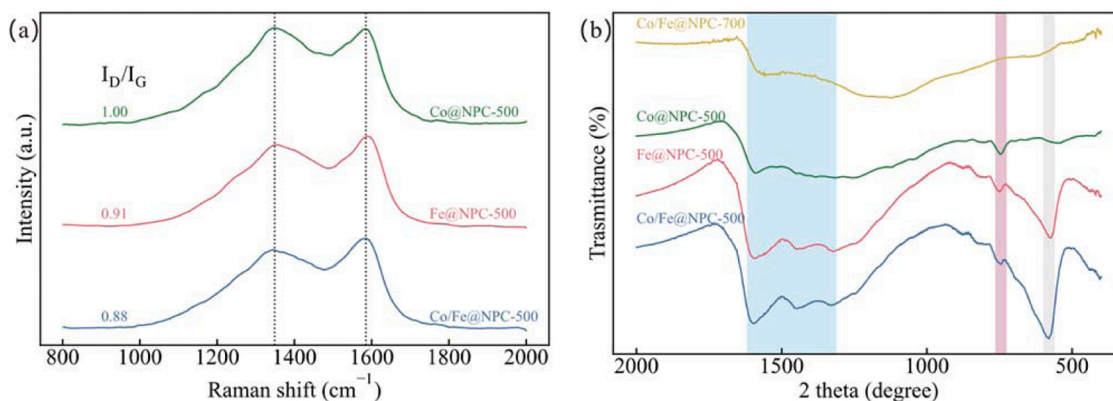

Fig. 4. (a) Raman spectra of Co/Fe@NPC-500, Fe@NPC-500, Co@NPC-500; (b) FT-IR spectra of Co/Fe@NPC-500, Fe@NPC-500, Co@NPC-500 and Co/Fe@NPC-700.

process.

The nitrogen adsorption/desorption isotherms and pore size distribution of the catalysts were shown in Fig. 45(a) and Fig. 45(b). When the calcination temperature was increased from 500 to 700 °C, the BET surface area of the materials decreased from 181.78 to 141.04 m^2 g^{-1} and the total pore volume decreased from 0.186 to 0.152 cm^3 g^{-1}, indicating that the structure of the catalysts calcined at 700 °C collapsed. The nitrogen adsorption/desorption isotherms of both Co/Fe@NPC-500 and Co/Fe@NPC-700 materials belonged to type IV isotherms with H4 hysteresis loops according to the IUPAC (International Union of Pure and Applied Chemistry) classification, indicating the presence of both micropores and mesopores [49]. And the mesoporous structure was conducive to the diffusive transport of both oxygen and electrolyte [50]. The pore size distribution could be seen that the pore sizes of both materials were mainly distributed around 2–30 nm, proving the hierarchical porous structure of microporous and mesoporous. Compared with Co/Fe@NPC-500, the pore capacity of Co/Fe@NPC-700 at 20 nm attachment decreased significantly, which also demonstrated that the high temperature calcination destroyed the structure of the material near the 20 nm pore structure Fig. 5.

3.2. Electrochemical performance

Cyclic voltammetry tests were performed in 10 mmol L^{-1} $K_3[Fe(CN)_6]$ and 1 mol L^{-1} KCl solutions with sweep rates ranging from 10 to 100 mV s^{-1} at a potential range from -0.2–0.6 V (vs. SCE). In Fig. 6(a), cyclic voltammetry curves were shown for Co/Fe@NPC-500 at different sweep rates, where the anodic peak current of the catalyst was linearly related to the square root of the scan rate, suggesting that the redox reaction was controlled by diffusion on the Co/Fe@NPC-500. Fig. 6(b) showed that the closed curve area of Co/Fe@NPC-500, Fe@NPC-500 and Co@NPC-500 were much larger than those of Co/Fe@PC-500, indicating that nitrogen doping enhanced the electrocatalytic activity areas of these catalysts. Additionally, it could be noted that the closed curve area of the monometallic catalysts (Fe@NPC-500 and Co@NPC-500) is approximately smaller than those of the bimetallic catalyst (Co/Fe@NPC-500). According to the Randles-Sevcik formula, the electrochemical surface area of Co/Fe@NPC-500, Fe@NPC-500, Co@NPC-500 and Co/Fe@PC-500 catalysts were calculated as 2.22×10^{-4}, 1.55×10^{-4}, 1.43×10^{-4} and 3.24×10^{-5} cm^2 respectively. As a result of the high graphitization of Co/Fe@NPC-500 and the synergistic effect of bimetallic catalysts, a significant increase in the electrochemical active area of Co/Fe@NPC-500 was obtained. The test results of ORR activity of Co/Fe@NPC-500 were shown in Fig. 6(c). A significant ORR peak current appeared on the CV curve under O_2-saturated condition compared to the curve under N_2-saturated conditions, suggesting that O_2 could be reduced on the catalyst surface. Based on the oxygen reduction curves of Co/Fe@NPC-500 and Co/Fe@PC-500 (Fig. S6), it could be proved that nitrogen doping could effectively improve the oxygen reduction ability of Co/Fe@NPC-500.

The EIS curves of all four catalysts in Fig. 6(d) consisted of a semicircle in the high-frequency region and a straight line in the low-frequency region, where the equivalent circuit included the solution resistance (Rs), the charge transfer resistance (Rct), the Warburg impedance (Wo) and the double capacitance [38]. Generally, the diameter of the semicircle directly correlates with the charge transfer resistance (Rct), so the smaller the diameter, the smaller the Rct. In comparison with Fe@NPC-500, Co/Fe@NPC-500 had a smaller charge transfer resistance, probably due to higher graphitization that accelerated electron transfer. Compared with Co/Fe@PC-500, the charge transfer resistance of nitrogen-doped catalyst was significantly reduced, proving that nitrogen could effectively reduce the electron transfer resistance and improve the electron transfer efficiency, which could also be seen from the smaller peak current of Co/Fe@PC-500 in the cyclic voltammetry test. Besides, it is the diffusion of electrolyte ions in the electrode materials that determines the slope of the curve in the low-frequency region. The higher the slope of the curve, the lower the diffusion resistance [51]. A low diffusion resistance of Co/Fe@PC-500 was evident from the EIS curve, which supported its ability to facilitate the diffusion of substances into the catalyst.

3.3. Mechanisms of low-valent metal formation

To explain the formation of low-valent metal during material preparation, three models had been proposed based on previous literature, Fe_3O_4 (I), Fe_3O_4-O-C (II) and Fe_3O_4-Co-O-C(III) [52,53].

Electrostatic potential distributions of model (II) and model (III) were shown in Fig. 7(a-b) where the region of low electron density (blue area) was located on C atoms of graphite, while the region of high electron density (red area) was located around Fe or Co. This difference in potential suggested there was a strong interaction between metal and carbon of graphite which would facilitate the transfer of electrons from C to the metal atoms.

Mulliken charge distribution was used to analyze charge transport paths and results were shown in Fig. 7(c-e). It could be found that Mulliken charge of Fe from Fe_3O_4 (I) to Fe_3O_4-Co-O-C (III) was gradually decreasing. Mulliken charge of Fe was reduced in Fe_3O_4-O-C(II) because of a large number of unpaired 2p orbital electrons on the carbon material which made it easy to transfer electrons from C atoms on graphite to Fe. And the result was also consistent with the electrostatic potential analysis. Compared with the Mulliken charge distribution in model 2, the Mulliken charge of Fe in model 3 decreased while the Mulliken charge of the C atom around the oxide increased, suggesting the presence of Co promoted the transfer of electrons from C atoms to Fe. Besides, the differential charge density diagram in Fig. 7(f) was used to analyze the role of Co during the formation of low-valent metals, where
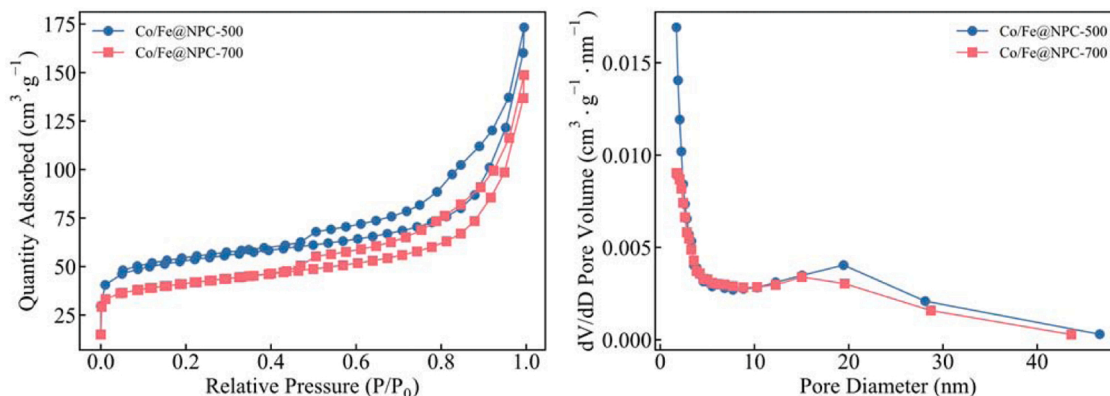

Fig. 5. (a) N_2 sorption isotherm and (b) pore size distribution for Co/Fe@NPC-500 and Co/Fe@NPC-700.
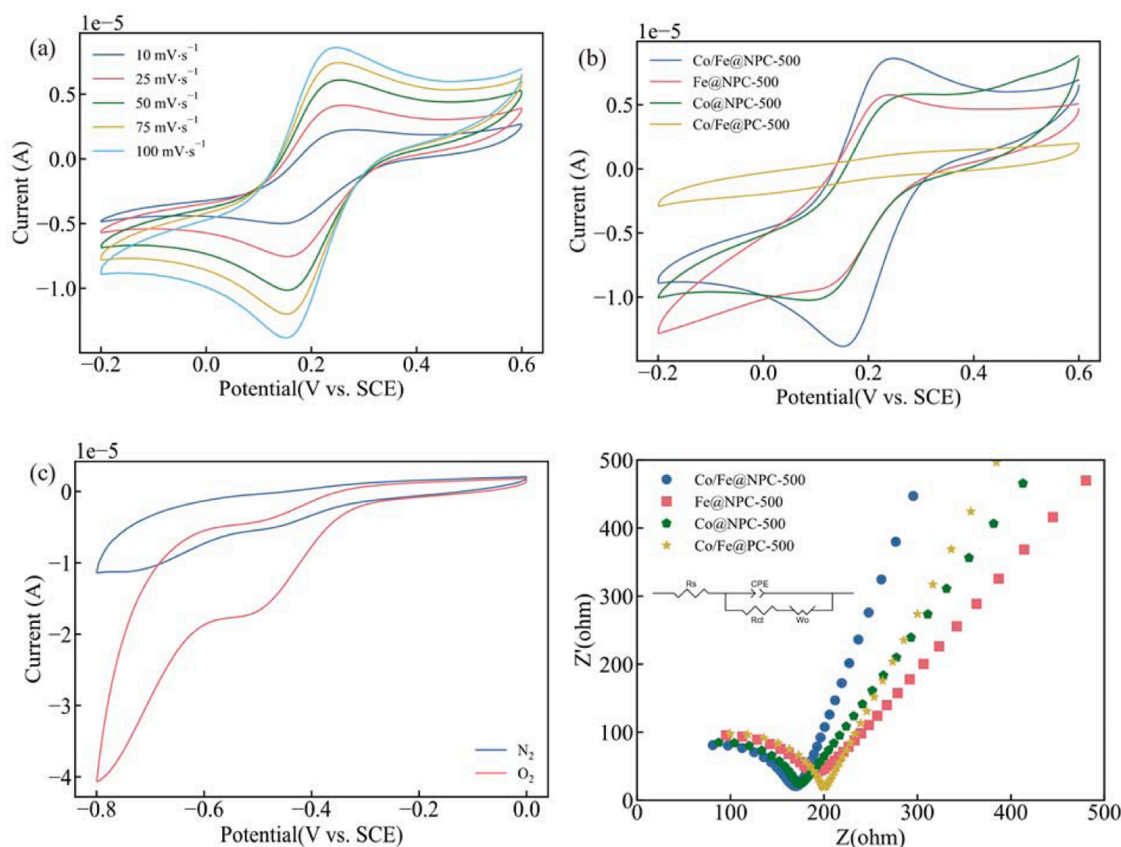
Fig. 6. CV curves of (a) Co/Fe@NPC-500 at various scan rates and (b) different catalysts at a scan rate of 10 mV s^{-1} in 10 mmol L^{-1} K$_3$[Fe(CN)$_6$] (1.0 mol L^{-1} KCl); (c) CV curves of Co/Fe@NPC-500 at 50 mV s^{-1} in 0.05 mol L^{-1} Na$_2$SO$_4$ solution under O$_2$/N$_2$ saturated condition; (d) EIS plots of different catalysts.

the green area represented where the electrons were obtained. It was clear that the addition of Co increased the electrons around Fe, which would promote the formation of Fe^{2+} and Fe^0. Based on the above results, it was speculated that Co could accelerate the transfer of electrons from C atoms of carbon material to Fe, thus increasing the content of low-valent metals in the material.

3.4. Degradation performance

The CAZ degradation efficiencies of the different cathodes obtained by calcination at 500 °C were shown in Fig. 8(a). It was clear that the CAZ degradation efficiency of the Co/Fe@NPC-500 (about 100%) was significantly higher in comparison with those of other cathodes (76.4% for Fe@NPC-500, 67.6% for Co@NPC-500, 61.4% for Co/Fe@NPC-500) in 90 min. Based on the characterization results, it was concluded that the highest CAZ removal rate could be obtained using Co/Fe@NPC-500 cathode probably due to the reduced interfacial transfer resistance by nitrogen doping, the synergistic effect of bimetal and the accelerated reduction of Fe^{3+} to Fe^{2+} by the lower valent metal.

The calcination temperature had a great influence on the performance of MOF derivatives. The low calcination temperature could lead to incomplete carbonization of the catalyst and thus reduce the electrical conductivity. However, the high calcination temperature could cause the collapse of the MOF structure, thus reducing the number of active sites. In this study, four calcination temperatures, 400, 500, 600 and 700 °C, were chosen for comparison, and the results were showed in Fig. 8(b). The removal efficiency of CAZ was 35.2%, 100%, 86.6% and 26.2% for the catalysts prepared at four calcination temperatures with primary reaction rate constants of 0.007, 0.087, 0.037 and 0.005 min^{-1}, respectively, where the best degradation performance of the MOF derivatives was prepared at 500 °C. This was mainly due to the low

proportion of divalent metals in the catalysts prepared at 400 °C, which was not favorable for the Fenton reaction. At temperatures above 600 °C, although high calcination temperature was beneficial to increase the proportion of low-valent metals in the catalysts, the structure of MOF derivatives also collapsed, affecting the degradation with the reduction of the active sites.

To optimize the current for degradation of CAZ in electro-Fenton, there were a range of different current values used for degradation experiments (Fig. 8(c)). The degradation efficiency of CAZ gradually increased with the increase of applied current from 10 to 80 mA. And CAZ was completely degraded in 30 min when the applied current reached 80 mA. This was mainly due to the fact that higher application current could effectively promote the production of H$_2$O$_2$ and accelerate the recycling of Fe$^{II/III}$ and Co$^{II/III}$, so the high current condition was beneficial to the degradation of CAZ [54]. However, the degradation efficiency of CAZ increased less when the applied current increased from 40 to 80 mA, mainly because the higher applied current would lead to the increase of side reactions such as hydrogen precipitation reaction [55]. In addition, the energy consumption at different application currents was calculated based on the applied current and voltage to evaluate the feasibility of degradation CAZ (Fig. 8(f)). W and E$_{EO}$ of CAZ were 16.0 and 5.1 kWh log^{-1} m^{-3} at 40 mA, respectively. According to the degradation effect and energy consumption of CAZ under different conditions, 40 mA was selected as the most suitable current for the following degradation experiments.

A study was conducted to determine how the catalyst would remove CAZ at different pH. As could be seen in Fig. 8(d), the removal efficiency of CAZ increased from 82% to complete degradation as the pH increased from 2 to 5, while the removal efficiency changed less with pH from 5 to 9. In general, under acidic conditions, the electro-Fenton system was more likely to produce H$_2$O$_2$, and the Fe$^{2+/3+}$ or Co$^{2+/3+}$ dissolved in the
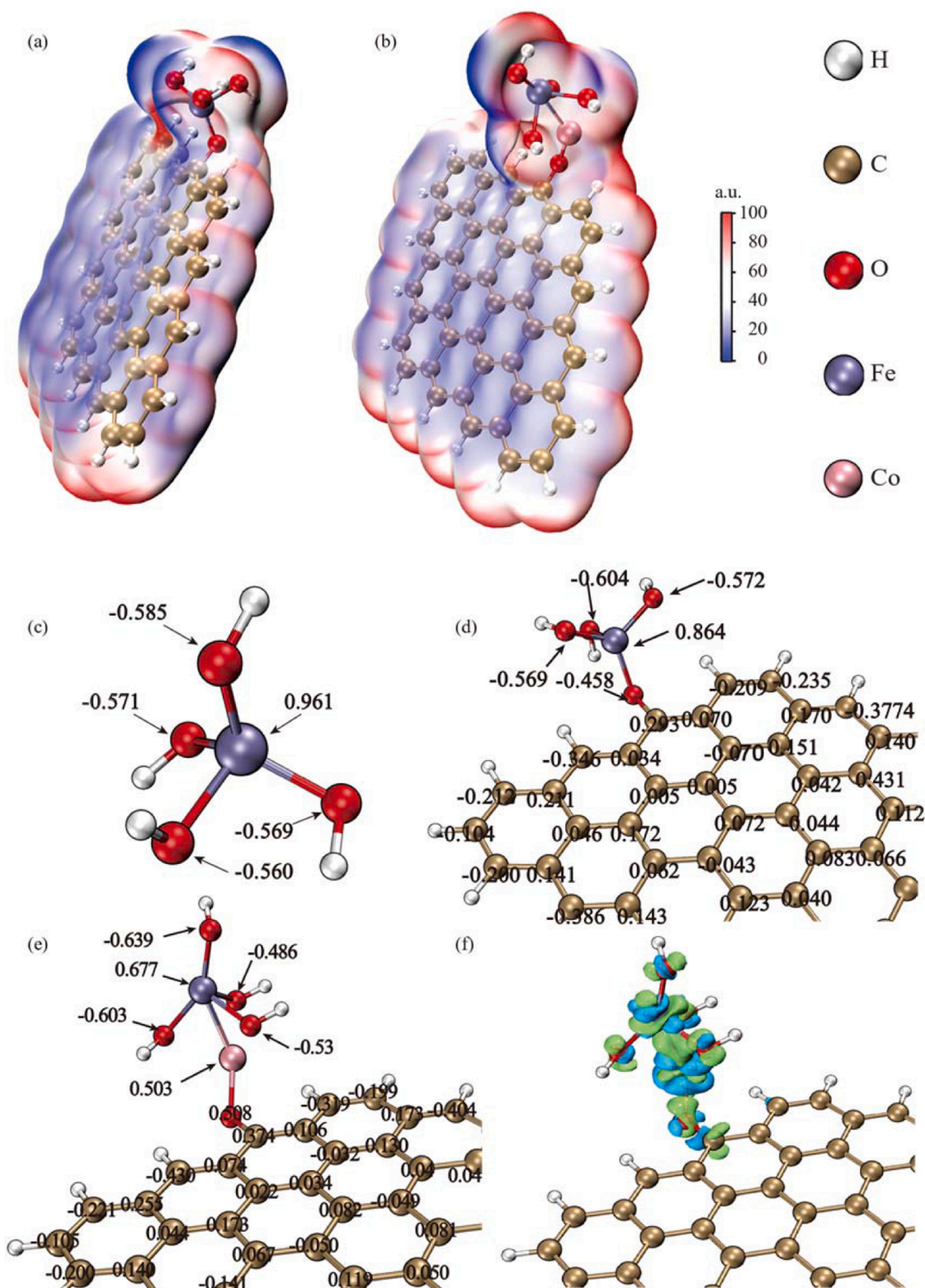
Fig. 7. Electrostatic potential distributions of (a) Fe_3O_4-O-C(II) and (b) Fe_3O_4-Co-O-C(III); Mulliken charge distribution of (c) Fe_3O_4, (d) Fe_3O_4-O-C and (e) Fe_3O_4-Co-O-C; (f) Differential charge density diagram of Fe_3O_4-Co-O-C.

solution could be used to activate H_2O_2 to generate free radicals [56]. However, CAZ degradation was less efficient under acidic than near-neutral conditions in this experiment, which could be assumed that the competing side reactions and loss of catalyst active sites at the electrode in the strongly acidic solution hindered the generation and

activation of H_2O_2 [36]. Overall, the degradation efficiency of CAZ could still reach a high level in acidic or neutral environments as a result of the strong electron transfer between the $Fe^{II/III}$ and $Co^{II/III}$ and in situ generation ·OH. The results showed that the catalyst could exhibit good removal ability of CAZ at a wide pH range.
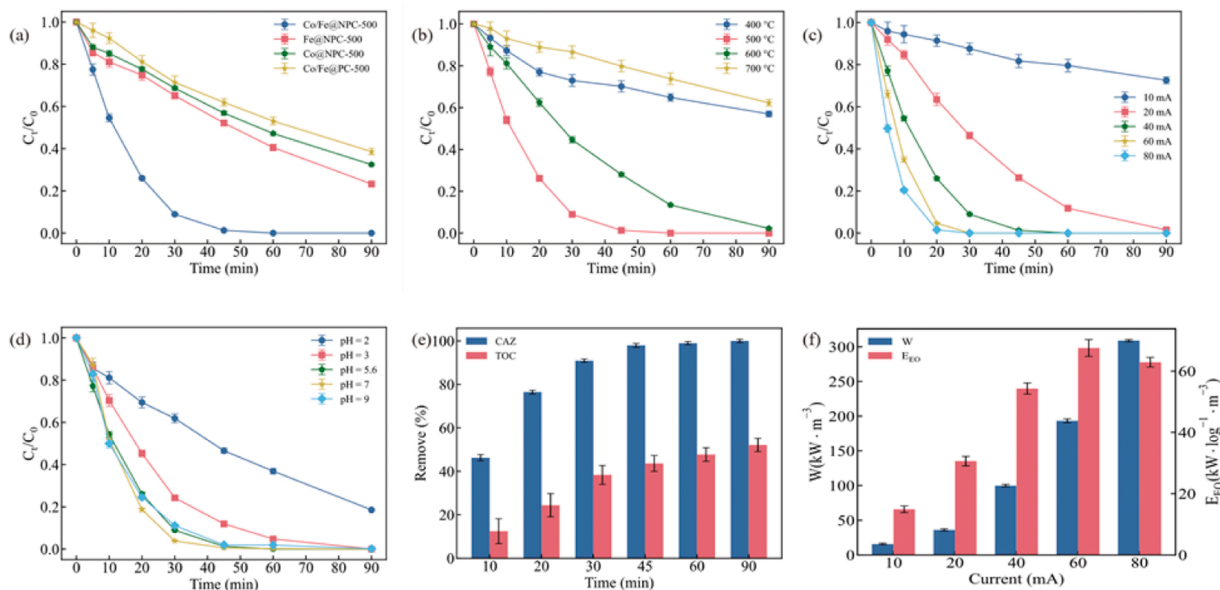
Fig. 8. The electro-Fenton degradation performance of CAZ for (a) different cathodes and for (b) Co/Fe@NPC cathodes calcined at various temperatures; The CAZ removal efficiency with Co/Fe@NPC-500 cathode under different conditions: (c) initial pH and (d) applied current; (f) The energy consumption under various applied currents; The removal efficiency of TOC (f); Unless otherwise stated, condition: [CAZ] = 5 mg L^{-1}, [Na$_2$SO$_4$] = 0.05 mol L^{-1}, applied current = 40 mA, pH = 5.6.

CAZ degradation experiment was conducted at initial concentrations of 1–9 mg L^{-1} to observe the effect of initial CAZ concentrations. It could be seen from Fig. S7 that the removal rates of CAZ decreased with an increase in initial concentrations of CAZ from 1 to 9 mg L^{-1}. It could be because the intermediates during the degradation of CAZ reacted with the active groups, which usually led to a decrease in the removal efficiency of CAZ [39].

The mineralization rate is a very important indicator in the removal of organic pollutants. As shown in Fig. 8(e), CAZ could be completely

removed while the removal rate of TOC was 52.1% in 90 min, which was attributed to the generation of other intermediates during the degradation of CAZ.

To investigate the feasibility of the Co/Fe@NPC-500 electro-Fenton system for the elimination of other antibiotics, different antibiotics were selected for degradation experiments, including sulfadiazine, tetracycline, ceftriaxone sodium and cefalexin. From Fig. S8, it was found that the removal rate of these pollutants was 88.8%, 91.8%, 100% and 89.0% in 90 min, indicating that the Co/Fe@NPC-500 electro-Fenton system
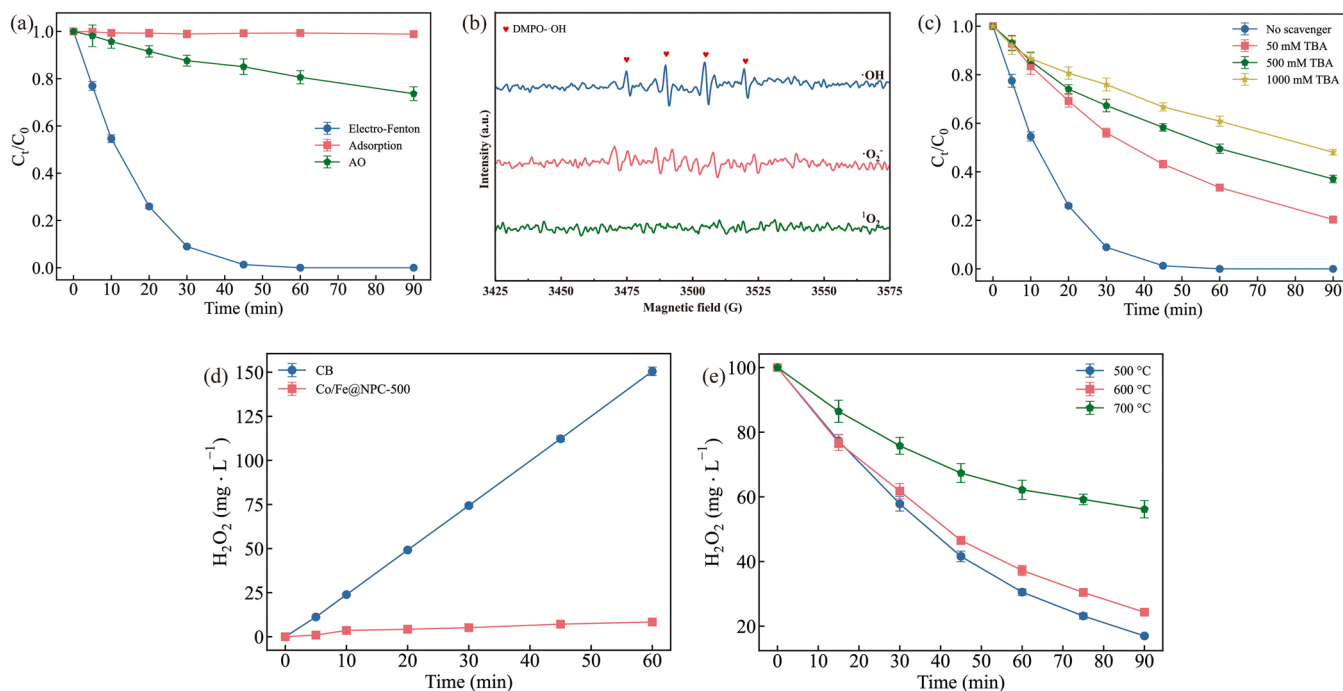

Fig. 9. (a) The CAZ removal performance in different systems; (b) EPR spectra of Co/Fe@NPC-500 cathode; (c)The CAZ degradation efficiency by TBA at various concentrations; (d) The H$_2$O$_2$ accumulation with different cathode; (e) decomposition of H$_2$O$_2$ with Co/Fe@NPC cathodes calcined at various temperatures; Conditions: [CAZ] = 5 mg L^{-1}, [Na$_2$SO$_4$] = 0.05 mol L^{-1}, applied current = 40 mA, pH = 5.6.

could effectively degrade a wide range of antibiotics.

3.5. Possible catalytic mechanism of CAZ removal

The removal of CAZ is mainly determined by the electro-Fenton reaction, anodic oxidation (AO) and adsorption [57]. In order to evaluate the contribution of each fraction in the removal of CAZ, we performed contaminant removal experiments in different systems as shown in Fig. 9 (a). The degradation efficiency of CAZ reached 19.4% and 100% in the anodic oxidation experiment with stainless-steel mesh as anode and electro-Fenton experiment, respectively. However, CAZ was almost not removed in the adsorption experiment. This indicated that the efficient removal of CAZ from the electro-Fenton reaction and anodic oxidation contributed to 19.4% and 80.6%, respectively. To explain the near zero contribution of adsorption to the removal of CAZ, the contact angle of the Co/Fe@NPC-500 cathode was measured in this study (Fig. S9). and the result indicated that the surface of this cathode with a contact angle of 112.4° was strongly hydrophobic which made it difficult for the hydrophilic CAZ to adsorb surface of the cathode [58].

Electron paramagnetic resonance (EPR) was used to identify reactive oxygen species in the electro-Fenton system and the results were displayed in Fig. 9(b). The characteristic quartet signal assigned to DMPO-·OH was detected in EPR with DMPO as the trapping agent of ·OH in EPR measurements [59]. Besides, it's found that the typical characteristic peaks of TEMP-$^1O_2$ and DMPO-·O_2^- did not appear on the EPR spectra, indicating they were not the main reactive oxygen species in this electro-Fenton system. Then, radical trapping experiments were performed in which TBA was used as the trapping agent for ·OH [9]. CAZ degradation was inhibited by the addition of 50 mmol L^{-1} TBA, and the degradation rate gradually decreased with the increase of the TBA concentration. Only 52% of the CAZ was removed after the addition of 1000 mmol L^{-1} TBA (Fig. 9(c)). Based on these results, ·OH was the main oxidizing agent for Co/Fe@NPC-500 electro-Fenton process.

As the electro-Fenton reaction mainly involves two processes of H_2O_2 production and activation, H_2O_2 accumulation and activation experiments were carried out. The H_2O_2 accumulation of Co/Fe@NPC-500 was only 8.3 mg L^{-1} lower than that of CB (Fig. 9(d)), which could be due to the rapid activation of the H_2O_2 generated in situ on the cathode into ·OH [36]. The H_2O_2 activation experiment was performed in a system containing a certain amount of H_2O_2 and the results were shown in Fig. 9(e). When the electrochemical reaction was carried out, the hydrogen peroxide started to decompose, where the remaining amount of hydrogen peroxide was 16 mg L^{-1} for Co/Fe@NPC-500, 24 mg L^{-1} for Co/Fe@NPC-600 and 56 mg L^{-1} for Co/Fe@NPC-700, respectively. This was in agreement with the results of the degradation experiments. Considering that ·OH was the main reactive species, we could infer that H_2O_2 in-situ generation would be activated to hydroxyl radicals on the electrode surface immediately.

Fig. S10 (a-b) showed the XPS spectra comparison of Co/Fe@NPC-500 cathode before and after the degradation experiment for Fe 2p and Co 2p. Notably, there was no significant change in the ratio of each valent state for either Fe or Co, which demonstrated the excellent cycling ability of the catalyst. After Fe^{II}/Co^{II} reacted with H_2O_2 to form Fe^{III}/Co^{III}, they could return to Fe^{II}/Co^{II} in the presence of Fe^0/Co^0 or electric current.

Based on the above results and discussion, a possible reaction mechanism was proposed for the degradation of CAZ with a Co/Fe@NPC cathode in the electro-Fenton system (Fig. 10). First, O_2 was adsorbed on the cathode surface and then H_2O_2 was generated in situ by a two-electron oxygen reduction process from O_2 (Eq. (7)). Subsequently, H_2O_2 was immediately activated by Fe^{II}/Co^{II} on the cathode surface to generate ·OH which could attack CAZ and other intermediates (Eq. (8)). Then Fe^{III}/Co^{III} would receive electrons from Fe^0 (Eqs. (9) – (12)) or from the cathode (Eq. (13)) to regenerate into Fe^{II}/Co^{II}, which was conducive to accelerate the cycle between Fe^{II}/Co^{II} and Fe^{III}/ Co^{III}. Besides, Co^{II} could also be regenerated by the reaction of Fe^{II} with Co^{III}
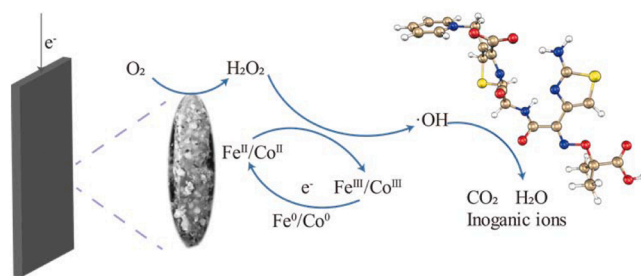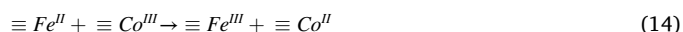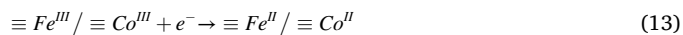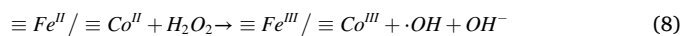

Fig. 10. Proposed mechanism of CAZ in electro-Fenton process with Co/Fe@NPC-500 cathode.

(Eq. (14)).

$$O_2 + 2e^- + 2H^+ \rightarrow H_2O_2 \tag{7}$$

$$\equiv Fe^{II}/\equiv Co^{II} + H_2O_2 \rightarrow \equiv Fe^{III}/\equiv Co^{III} + \cdot OH + OH^- \tag{8}$$

$$\equiv Fe^0 + 2 \equiv Fe^{III} \rightarrow 3 \equiv Fe^{II} \tag{9}$$

$$Fe^0 + 2 \equiv Co^{III} \rightarrow 2 \equiv Co^{II} + \equiv Fe^{II} \tag{10}$$

$$Co^0 + 2 \equiv Co^{III} \rightarrow 3 \equiv Co^{II} \tag{11}$$

$$Co^0 + 2 \equiv Fe^{III} \rightarrow 2 \equiv Fe^{II} + \equiv Co^{II} \tag{12}$$

$$\equiv Fe^{III}/\equiv Co^{III} + e^- \rightarrow \equiv Fe^{II}/\equiv Co^{II} \tag{13}$$

$$\equiv Fe^{II} + \equiv Co^{III} \rightarrow \equiv Fe^{III} + \equiv Co^{II} \tag{14}$$

3.6. Reusability evaluation of electrode

The stability of the electro-Fenton system was a critical factor for practical applications. After eight consecutive degradation cycles, the removal efficiency of CAZ illustrated in Fig. 11(a) still reached more than 90.6%, which indicated that there was little loss of active sites on the catalyst surface during the degradation process. Besides, as shown in Fig. 11(b), there was no obvious change in the XRD patterns of the electrode before and after use, which demonstrates the stability of the electrode. The Fig. S11 showed the Co and Fe leached from the catalyst in the stability test, where the maximum leaching of Fe and Co was 0.02 and 0.4 mg L^{-1}, lower the limits of European Union standard (Fe < 2 mg L^{-1}) and water environment discharge standards of China (Co < 1 mg L^{-1}) (GB 25467–2010), respectively. The above results demonstrated that the Co/Fe@NPC-500 cathode had good stability compared with other MOF-derived cathodes summarized in Table S1.

3.7. CAZ site evaluation and degradation pathway

The DFT calculation of CAZ was performed to determine the reaction sites of CAZ with·OH during the electro-Fenton process. Fig. 12(a) showed the chemical structure of CAZ after geometry optimization. The results of the highest occupied molecular orbital (HOMO) suggested that the thiazole ring in CAZ was the most susceptible to losing electrons, which·OH as electrophilic radicals preferred to attack (Fig. 12(b)). In addition, the Fukui index of f^-, f^+ and f^0 represented electrophilic, nucleophilic and free radical reactions, respectively [60]. It's reported that the sites with high f^- or f^0 were the most reactive [61], which could theoretically reveal the reactive sites of CAZ molecules (Fig. 12(c)). Similar to the result of HOMO, the thiazole ring on CAZ tended to fall off. Because those sites located on the thiazole ring, S12 ($f^0 = 0.0789$, $f^- = 0.1556$), N15 ($f^0 = 0.0648$, $f^- = 0.1293$), C11 ($f^0 = 0.0637$, $f^- = 0.1268$) and C10 ($f^0 = 0.0432$, $f^- = 0.0863$), had the high Fukui index of f^0 or f^-. Besides, some sites not on the thiazole ring could also be attacked, such
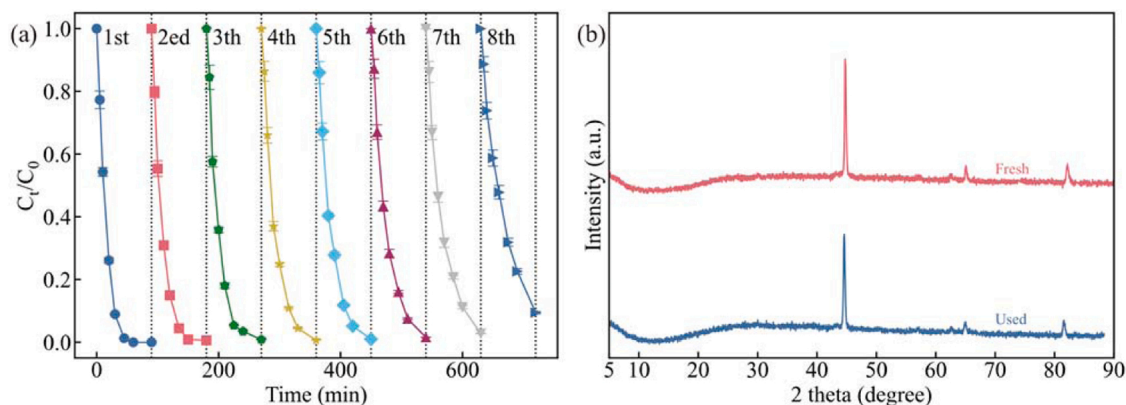
Fig. 11. (a) Cycling stability of Co/Fe@NPC-500 cathode for CAZ removal; and (b) XRD patterns of Co/Fe@NPC-500 cathode before and after the degradation experiment.
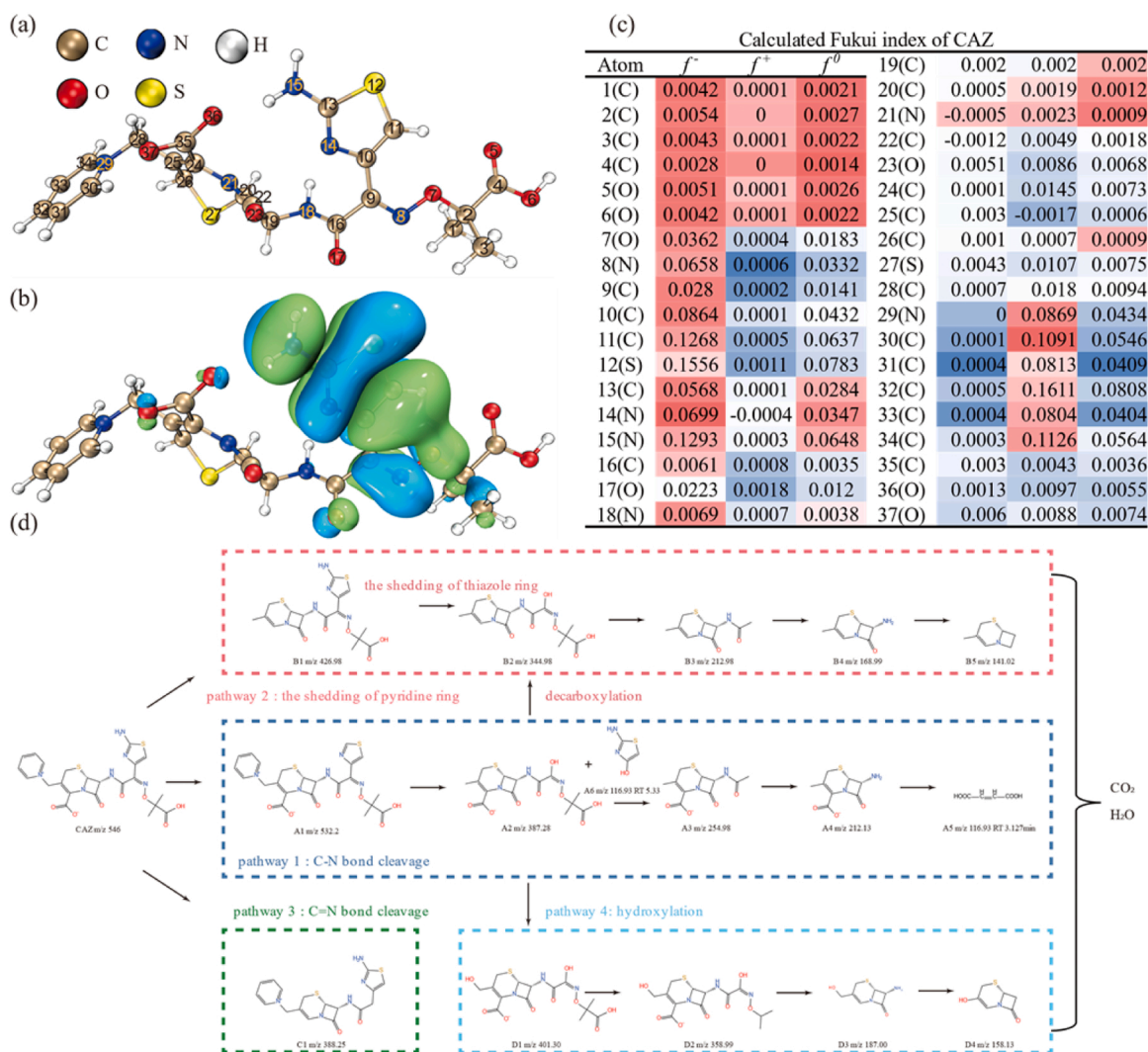

Fig. 12. (a) Chemical structure of CAZ; (b) HOMO of CAZ; (c) Fukui index of CAZ; (d) proposed degradation pathway of CAZ in Co/Fe@NPC-500 electro-Fenton system.

as N29 ($f^0 = 0.0434$) and N8 ($f^0 = 0.0332$, $f^- = 0.0658$). Based on the results of DFT calculations and LC-MS (Fig. S12), four degradation pathways of CAZ are proposed (Fig. 12(d)). In pathway 1, the N15 of CAZ was attacked by·OH with C-N bond cleavage to form products A1, corresponding to the Fukui index of N15 ($f^0 = 0.0648$, $f^- = 0.1293$).

Then, the pyridine ring and the thiazole of product A1 were attacked by·OH to form products A2 and A6, which were agreement with the high Fukui index of N29 ($f^0 = 0.0434$) and C10 ($f^0 = 0.0432$, $f^- = 0.0863$). Product A2 could enter pathway 3 and pathway 4 through decarboxylation and hydroxylation with the formation of Products B2 and E1.

Products A2, B2 and E1 gradually changed from large molecules to small molecules through continuous bond breaking until it was completely mineralized. In pathway 2 of the shedding of the pyridine ring, N29 ($f^0 = 0.0434$) was attacked, which led to the C-N bond was broken with the formation of Product B1. Besides, Product B1 could be converted to B2 by the shedding of the thiazole ring. Product C1 was produced by the cleavage of the C=N bond and decarboxylation in the pathway 3, which were attributed to the high Fukui index of N8 ($f^0 = 0.0332$, $f^- = 0.0658$). Four degradation pathways of CAZ in Co/Fe@NPC-500 electro-Fenton system through the shedding of the pyridine ring and the thiazole, bond cleavage, decarboxylation and hydroxylation were proposed based on the identification of intermediates and the Fukui index.

4. Conclusions

In this study, a MOF-derived carbon material containing CoFe alloy (Co/Fe@NPC-500) by calcining Co/Fe bimetallic MOF with N-doped at a lower temperature was successfully synthesized. The addition of Co resulted in the formation of a large number of low-valent metals while maintaining the original structure of the MOF. Thanks to the synergistic effect of bimetallic and nitrogen doping, Co/Fe@NPC-500 achieved superior electrochemical properties compared to other materials. In the degradation experiments, Co/Fe@NPC-500 cathode showed excellent degradation ability for CAZ at a wide pH range. Besides, ·OH was found to be the main active species by EPR and quenching experiments. Finally, based on the results of HPLC-MS and DFT calculations, the degradation pathway of CAZ was proposed. This study provides a strategy to prepare MOF-derived carbon materials containing low-valent metals for electro-Fenton reactions while maintaining the MOF structure.

CRediT authorship contribution statement

Hexiang Wang: Data curation, Investigation, Formal analysis, Writing – original draft preparation. **Chenliu Tang**: Formal analysis, Writing – review & editing. **Luwei Wang:** Data curation, Formal analysis. **Zhirong Sun:** Conceptualization, Methodology, Writing – review & editing. **Xiang Hu**: Funding acquisition, Supervision, Conceptualization, Methodology, Writing – review & editing, Project administration.

Declaration of Competing Interest

The authors declare that they have no known competing financial interests or personal relationships that could have appeared to influence the work reported in this paper.

Data Availability

Data will be made available on request.

Acknowledgements

Appendix A. Supporting information

Supplementary data associated with this article can be found in the online version at doi:10.1016/j.apcatb.2023.122755.

References

[1] P. Kovalakova, L. Cizmas, T.J. McDonald, B. Marsalek, M. Feng, V.K. Sharma, Occurrence and toxicity of antibiotics in the aquatic environment: a review, Chemosphere 251 (2020), 126351, https://doi.org/10.1016/j.chemosphere.2020.126351.

[2] P. Duan, S. Gao, J. Lei, X. Li, X. Hu, Electrochemical oxidation of ceftazidime with graphite/CNT-Ce/PbO₂–Ce anode: Parameter optimization, toxicity analysis and degradation pathway, Environ. Pollut. 263 (2020) 114436, https://doi.org/10.1016/j.envpol.2020.114436.

[3] W. Wang, H. Wang, W. Zhang, H. Liang, D. Gao, Occurrence, distribution, and risk assessment of antibiotics in the Songhua River in China, Environ. Sci. Pollut. Res. 24 (2017) 19282–19292, https://doi.org/10.1007/s11356-017-9471-x.

[4] Y. Zhu, W. Fan, W. Feng, Y. Wang, S. Liu, Z. Dong, X. Li, A critical review on metal complexes removal from water using methods based on Fenton-like reactions: Analysis and comparison of methods and mechanisms, J. Hazard. Mater. 414 (2021), 125517, https://doi.org/10.1016/j.jhazmat.2021.125517.

[5] Z. Ye, J.A. Padilla, E. Xuriguera, J.L. Beltran, F. Alcaide, E. Brillas, I. Sirés, A highly stable metal–organic framework-engineered FeS₂/C nanocatalyst for Heterogeneous electro-Fenton treatment: Validation in wastewater at mild pH, Environ. Sci. Technol. 54 (2020) 4664–4674, https://doi.org/10.1021/acs.est.9b07604.

[6] C.M. Oliva González, B.I. Kharisov, O.V. Kharissova, T.E.Serrano Quezada, Synthesis and applications of MOF-derived nanohybrids: a review, Mater. Today.: Proc. 46 (2021) 3018–3029, https://doi.org/10.1016/j.matpr.2020.12.1231.

[7] D. Huang, G. Wang, M. Cheng, G. Zhang, S. Chen, Y. Liu, Z. Li, W. Xue, L. Lei, R. Xiao, Optimal preparation of catalytic metal-organic framework derivatives and their efficient application in advanced oxidation processes, Chem. Eng. J. 421 (2021), 127817, https://doi.org/10.1016/j.cej.2020.127817.

[8] H. Zhao, Y. Chen, Q. Peng, Q. Wang, G. Zhao, Catalytic activity of MOF(2Fe/Co)/carbon aerogel for improving H₂O₂ and·OH generation in solar photo–electro–Fenton process, Appl. Catal. B Environ. 203 (2017) 127–137, https://doi.org/10.1016/j.apcatb.2016.09.074.

[9] S. Cheng, C. Shen, H. Zheng, F. Liu, A. Li, OCNTs encapsulating Fe-Co PBA as efficient chainmail-like electrocatalyst for enhanced heterogeneous electro-Fenton reaction, Appl. Catal. B Environ. 269 (2020) 118785, https://doi.org/10.1016/j.apcatb.2020.118785.

[10] C. Liu, Y. Wang, Y. Zhang, R. Li, W. Meng, Z. Song, F. Qi, B. Xu, W. Chu, D. Yuan, B. Yu, Enhancement of Fe@porous carbon to be an efficient mediator for peroxymonosulfate activation for oxidation of organic contaminants: Incorporation NH₂-group into structure of its MOF precursor, Chem. Eng. J. 354 (2018) 835–848, https://doi.org/10.1016/j.cej.2018.08.060.

[11] P. Dong, H. Wang, W. Liu, S. Wang, Y. Wang, J. Zhang, F. Lin, Y. Wang, C. Zhao, X. Duan, S. Wang, H. Sun, Quasi-MOF derivative-based electrode for efficient electro-Fenton oxidation, J. Hazard. Mater. 401 (2021), 123423, https://doi.org/10.1016/j.jhazmat.2020.123423.

[12] P. Cao, K. Zhao, X. Quan, S. Chen, H. Yu, Efficient and stable heterogeneous electro-Fenton system using iron oxides embedded in Cu, N co-doped hollow porous carbon as functional electrocatalyst, Sep. Purif. Technol. 238 (2020), 116424, https://doi.org/10.1016/j.seppur.2019.116424.

[13] L. He, F. Weniger, H. Neumann, M. Beller, Synthesis, characterization, and application of metal nanoparticles supported on nitrogen-doped carbon: Catalysis beyond electrochemistry, Angew. Chem. Int. Ed. 55 (2016) 12582–12594, https://doi.org/10.1002/anie.201603198.

[14] D.-H. Xie, P.-C. Guo, K.-Q. Zhong, G.-P. Sheng, Highly dispersed Co/Fe bimetal in carbonaceous cages as heterogeneous Fenton nanocatalysts for enhanced sulfamethoxazole degradation, Appl. Catal. B Environ. 319 (2022), 121923, https://doi.org/10.1016/j.apcatb.2022.121923.

[15] R.M. Sellers, Spectrophotometric determination of hydrogen peroxide using potassium titanium(IV) oxalate, Analyst 105 (1980) 950–954, https://doi.org/10.1039/an9800500950.

[16] H. Zhang, Y. Li, G. Li, F. Zhang, Scaling up floating air cathodes for energy-efficient H₂O₂ generation and electrochemical advanced oxidation processes, Electrochim. Acta 299 (2019) 273–280, https://doi.org/10.1016/j.electacta.2019.01.010.

[17] F. Weigend, R. Ahlrichs, Balanced basis sets of split valence, triple zeta valence and quadruple zeta valence quality for H to Rn: Design and assessment of accuracy, Phys. Chem. Chem. Phys. 7 (2005) 3297–3305, https://doi.org/10.1039/B508541A.

[18] F. Weigend, Accurate Coulomb-fitting basis sets for H to Rn, Phys. Chem. Chem. Phys. 8 (2006) 1057–1065, https://doi.org/10.1039/B515623H.

[19] S. Grimme, J. Antony, S. Ehrlich, H. Krieg, A consistent and accurate ab initio parametrization of density functional dispersion correction (DFT-D) for the 94 elements H-Pu, J. Chem. Phys. 132 (2010), 154104, https://doi.org/10.1063/1.3382344.

[20] S. Grimme, S. Ehrlich, L. Goerigk, Effect of the damping function in dispersion corrected density functional theory, J. Comput. Chem. 32 (2011) 1456–1465, https://doi.org/10.1002/jcc.21759.

[21] A.D. Becke, A new mixing of Hartree–Fock and local density-functional theories, J. Chem. Phys. 98 (1993) 1372–1377, https://doi.org/10.1063/1.464304.

[22] P.C. Hariharan, J.A. Pople, The influence of polarization functions on molecular orbital hydrogenation energies, Theor. Chim. Acta 28 (1973) 213–222, https://doi.org/10.1007/BF00533485.

[23] M.J. Frisch, J.A. Pople, J.S. Binkley, Self-consistent molecular orbital methods 25. Supplementary functions for Gaussian basis sets, J. Chem. Phys. 80 (1984) 3265–3269, https://doi.org/10.1063/1.447079.

[24] F. Neese, The ORCA program system, WIREs Comput. Mol. Sci. 2 (2012) 73–78, https://doi.org/10.1002/wcms.81.

[25] F. Neese, Software update: the ORCA program system—Version 5.0, WIREs Comput. Mol. Sci. 12 (2022), e1606, https://doi.org/10.1002/wcms.1606.

[26] T. Lu, F. Chen, Multiwfn: A multifunctional wavefunction analyzer, J. Comput. Chem. 33 (2012) 580–592, https://doi.org/10.1002/jcc.22885.

[27] T. Lu, Q. Chen, Realization of conceptual density functional theory and information-theoretic approach in Multiwfn Program, in: S. Liu (Ed.), Conceptual Density Functional Theory, first ed., Wiley, 2022, pp. 631–647, https://doi.org/10.1002/9783527829941.ch31.

[28] T. Lu, F. Chen, Quantitative analysis of molecular surface based on improved marching tetrahedra algorithm, J. Mol. Graph. Model. 38 (2012) 314–323, https://doi.org/10.1016/j.jmgm.2012.07.004.

[29] W. Humphrey, A. Dalke, K. Schulten, VMD: Visual molecular dynamics, J. Mol. Graph. 14 (1996) 33–38, https://doi.org/10.1016/0263-7855(96)00018-5.

[30] S. Bauer, C. Serre, T. Devic, P. Horcajada, J. Marrot, G. Férey, N. Stock, High-throughput assisted rationalization of the formation of metal organic frameworks in the Iron(III) aminoterephthalate solvothermal system, Inorg. Chem. 47 (2008) 7568–7576, https://doi.org/10.1021/ic800538r.

[31] D. Bara, E.G. Meekel, I. Pakamorė, C. Wilson, S. Ling, R.S. Forgan, Exploring and expanding the Fe-terephthalate metal–organic framework phase space by coordination and oxidation modulation, Mater. Horiz. 8 (2021) 3377–3386, https://doi.org/10.1039/D1MH01663F.

[32] W. Wong-Ng, J.A. Kaduk, H. Wu, M. Suchomel, Synchrotron X-ray studies of metal-organic framework M_2 (2,5-dihydroxyterephthalate), M= (Mn, Co, Ni, Zn) (MOF74), Powder Diffr. 27 (2012) 256–262, https://doi.org/10.1017/S0885715612000863.

[33] C.B.L. Tschense, N. Reimer, C.-W. Hsu, H. Reinsch, R. Siegel, W.-J. Chen, C.-H. Lin, A. Cadiau, C. Serre, J. Senker, N. Stock, New group 13 MIL-53 derivates based on 2,5–thiophenedicarboxylic acid, Z. Anorg. Allg. Chem. 643 (2017) 1600–1608, https://doi.org/10.1002/zaac.201700260.

[34] J. Huang, X. Zhang, H. Song, C. Chen, F. Han, C. Wen, Protonated graphitic carbon nitride coated metal-organic frameworks with enhanced visible-light photocatalytic activity for contaminants degradation, Appl. Surf. Sci. 441 (2018) 85–98, https://doi.org/10.1016/j.apsusc.2018.02.027.

[35] Q. Huang, L. Zhao, G. Zhu, D. Chen, X. Ma, X. Yang, S. Wang, Outstanding performance of thiophene-based metal-organic frameworks for fluoride capture from wastewater, Sep. Purif. Technol. 298 (2022), 121567, https://doi.org/10.1016/j.seppur.2022.121567.

[36] S. Qiu, Y. Wang, J. Wan, Y. Ma, Z. Yan, S. Yang, Enhanced electro-Fenton catalytic performance with in-situ grown Ce/Fe@NPC-GF as self-standing cathode: fabrication, influence factors and mechanism, Chemosphere 273 (2021), 130269, https://doi.org/10.1016/j.chemosphere.2021.130269.

[37] Z. Yang, L. Zhang, Y. Zhang, M. Bai, Y. Zhang, Z. Yue, E. Duan, Effects of apparent activation energy in pyrolytic carbonization on the synthesis of MOFs-carbon involving thermal analysis kinetics and decomposition mechanism, Chem. Eng. J. 395 (2020), 124980, https://doi.org/10.1016/j.cej.2020.124980.

[38] P.J.M. Cordeiro-Junior, M.S. Kronka, L.A. Goulart, N.C. Veríssimo, L.H. Mascaro, M.C. dos Santos, R. Bertazzoli, M.R.V. Lanza, Catalysis of oxygen reduction reaction for H_2O_2 electrogeneration: the impact of different conductive carbon matrices and their physicochemical properties, J. Catal. 392 (2020) 56–68, https://doi.org/10.1016/j.jcat.2020.09.020.

[39] X. Zhou, D. Xu, Y. Chen, Y. Hu, Enhanced degradation of triclosan in heterogeneous E-Fenton process with MOF-derived hierarchical Mn/Fe@PC modified cathode, Chem. Eng. J. 384 (2020), 123324, https://doi.org/10.1016/j.cej.2019.123324.

[40] L. Deng, M. Zhu, Metal–nitrogen (Co-g-C_3N_4) doping of surface-modified single-walled carbon nanohorns for use as an oxygen reduction electrocatalyst, RSC Adv. 6 (2016) 25670–25677, https://doi.org/10.1039/C5RA27895C.

[41] P. Cao, X. Quan, K. Zhao, S. Chen, H. Yu, J. Niu, Selective electrochemical H_2O_2 generation and activation on a bifunctional catalyst for heterogeneous electro-Fenton catalysis, J. Hazard. Mater. 382 (2020), 121102, https://doi.org/10.1016/j.jhazmat.2019.121102.

[42] Y. Zhou, Y. Zhang, X. Hu, Synergistic coupling Co_3Fe_7 alloy and $CoFe_2O_4$ spinel for highly efficient removal of 2,4-dichlorophenol by activating peroxymonosulfate, Chemosphere 242 (2020), 125244, https://doi.org/10.1016/j.chemosphere.2019.125244.

[43] W. Zhang, X. Jiang, X. Wang, Y.V. Kaneti, Y. Chen, J. Liu, J.-S. Jiang, Y. Yamauchi, M. Hu, Spontaneous weaving of graphitic carbon networks synthesized by pyrolysis of ZIF-67 crystals, Angew. Chem. Int. Ed. 56 (2017) 8435–8440, https://doi.org/10.1002/anie.201701252.

[44] M. Jiang, C. Fu, R. Cheng, W. Zhang, T. Liu, R. Wang, J. Zhang, B. Sun, Integrated and binder-free air cathodes of Co_3Fe_7 nanoalloy and $Co_{5.74}N$ encapsulated in nitrogen-doped carbon foam with superior oxygen reduction activity in flexible aluminum-air batteries, Adv. Sci. 7 (2020) 2000747, https://doi.org/10.1002/advs.202000747.

[45] M. Hao, M. Qiu, H. Yang, B. Hu, X. Wang, Recent advances on preparation and environmental applications of MOF-derived carbons in catalysis, Sci. Total Environ. 760 (2021), 143333, https://doi.org/10.1016/j.scitotenv.2020.143333.

[46] S. Fu, C. Zhu, J. Song, D. Du, Y. Lin, Metal-organic framework-derived non-precious metal nanocatalysts for oxygen reduction reaction, Adv. Energy Mater. 7 (2017) 1700363, https://doi.org/10.1002/aenm.20170036.

[47] X. Du, W. Fu, P. Su, J. Cai, M. Zhou, Internal-micro-electrolysis-enhanced heterogeneous electro-Fenton process catalyzed by Fe/Fe_3C@PC core–shell hybrid for sulfamethazine degradation, Chem. Eng. J. 398 (2020), 125681, https://doi.org/10.1016/j.cej.2020.125681.

[48] L. Cui, H. Huang, P. Ding, S. Zhu, W. Jing, X. Gu, Cogeneration of H_2O_2 and ·OH via a novel Fe_3O_4/MWCNTs composite cathode in a dual-compartment electro-Fenton membrane reactor, Sep. Purif. Technol. 237 (2020), 116380, https://doi.org/10.1016/j.seppur.2019.116380.

[49] M. Thommes, K. Kaneko, A. Neimark, J.P. Olivier, F. Rodriguez-Reinoso, J. Rouquerol, K.S.W. Sing, Physisorption of gases, with special reference to the evaluation of surface area and pore size distribution (IUPAC Technical Report), Pure Appl. Chem. 87 (2015) 1051–1069, https://doi.org/10.1515/pac-2014-1117.

[50] N. Fernández-Sáez, D.E. Villela-Martinez, F. Carrasco-Marín, A.F. Pérez-Cadenas, L. M. Pastrana-Martínez, Heteroatom-doped graphene aerogels and carbon-magnetite catalysts for the heterogeneous electro-Fenton degradation of acetaminophen in aqueous solution, J. Catal. 378 (2019) 68–79, https://doi.org/10.1016/j.jcat.2019.08.020.

[51] H.H. Dang, D.T.C. Nguyen, T.T. Nguyen, T.T.T. Nguyen, D.-V.N. Vo, T.D. Nguyen, T. Lee, T.V. Tran, Zeolitic-imidazolate framework-derived N-self-doped porous carbons with ultrahigh theoretical adsorption capacities for tetracycline and ciprofloxacin, J. Environ. Chem. Eng. 9 (2021), 104938, https://doi.org/10.1016/j.jece.2020.104938.

[52] J. Chen, J. Wan, C. Li, Y. Wei, H. Shi, Synthesis of novel Fe^0-Fe_3O_4/CeO_2/C composite cathode for efficient heterogeneous electro-Fenton degradation of ceftriaxone sodium, J. Hazard. Mater. 437 (2022), 129393, https://doi.org/10.1016/j.jhazmat.2022.129393.

[53] X. Zhang, Z. Yao, Y. Zhou, Z. Zhang, G. Lu, Z. Jiang, Theoretical guidance for the construction of electron-rich reaction microcenters on C–O–Fe bridges for enhanced Fenton-like degradation of tetracycline hydrochloride, Chem. Eng. J. 411 (2021), 128535, https://doi.org/10.1016/j.cej.2021.128535.

[54] Z.-J. Liu, J.-Q. Wan, Z.-C. Yan, Y. Wang, Y.-W. Ma, Efficient removal of ciprofloxacin by heterogeneous electro-Fenton using natural air–cathode, Chem. Eng. J. 433 (2022), 133767, https://doi.org/10.1016/j.cej.2021.133767.

[55] P. Dong, X. Chen, M. Guo, Z. Wu, H. Wang, F. Lin, J. Zhang, S. Wang, C. Zhao, H. Sun, Heterogeneous electro-Fenton catalysis with self-supporting CFP@MnO2-Fe_3O_4/C cathode for shale gas fracturing flowback wastewater, J. Hazard. Mater. 412 (2021), 125208, https://doi.org/10.1016/j.jhazmat.2021.125208.

[56] L. Cui, Z. Li, Q. Li, M. Chen, W. Jing, X. Gu, Cu/$CuFe_2O_4$ integrated graphite felt as a stable bifunctional cathode for high-performance heterogeneous electro-Fenton oxidation, Chem. Eng. J. 420 (2021), 127666, https://doi.org/10.1016/j.cej.2020.127666.

[57] T. Cui, Z. Xiao, Z. Wang, C. Liu, Z. Song, Y. Wang, Y. Zhang, R. Li, B. Xu, F. Qi, A. Ikhlaq, FeS_2/carbon felt as an efficient electro-Fenton cathode for carbamazepine degradation and detoxification: In-depth discussion of reaction contribution and empirical kinetic model, Environ. Pollut. 282 (2021), 117023, https://doi.org/10.1016/j.envpol.2021.117023.

[58] I.V. Tetko, J. Gasteiger, R. Todeschini, A. Mauri, D. Livingstone, P. Ertl, V. A. Palyulin, E.V. Radchenko, N.S. Zefirov, A.S. Makarenko, V.V. V.Yu. Tanchuk, Prokopenko, Virtual computational chemistry laboratory – Design and description, J. Comput. Aided Mol. Des. 19 (2005) 453–463, https://doi.org/10.1007/s10822-005-8694-y.

[59] Z. Ye, G.E.M. Schukraft, A. L'Hermitte, Y. Xiong, E. Brillas, C. Petit, I. Sirés, Mechanism and stability of an Fe-based 2D MOF during the photoelectro-Fenton treatment of organic micropollutants under UVA and visible light irradiation, Water Res. 184 (2020), 115986, https://doi.org/10.1016/j.watres.2020.115986.

[60] A. Wang, J. Ni, W. Wang, D. Liu, Q. Zhu, B. Xue, C.-C. Chang, J. Ma, Y. Zhao, MOF derived Co—Fe nitrogen doped graphite carbon@crosslinked magnetic chitosan micro–nanoreactor for environmental applications: Synergy enhancement effect of adsorption—PMS activation, Appl. Catal. B Environ. 319 (2022), 121926, https://doi.org/10.1016/j.apcatb.2022.121926.

[61] J. Qi, X. Yang, P.-Y. Pan, T. Huang, X. Yang, C.-C. Wang, W. Liu, Interface engineering of $Co(OH)_2$ nanosheets growing on the $KNbO_3$ perovskite based on electronic structure modulation for enhanced peroxymonosulfate activation, Environ. Sci. Technol. 56 (2022) 5200–5212, https://doi.org/10.1021/acs.est.1c08806.